Measurement Reliability and Functional Validity of Bruch's Membrane Calcification in Pseudoxanthoma Elasticum: PROPXE Study Report 2

Jason A. W. Giger,[1] Georg Ansari,[1] Sharon F. Terry,[2] Peter Charbel Issa,[3] Kristina Pfau,[1,4] and Maximilian Pfau[1,4]; for the PROPXE Study Group

[1]Department of Ophthalmology, University of Basel, Basel, Switzerland
[2]PXE International, Washington, DC, United States
[3]Technical University of Munich, School of Medicine and Health, Department of Ophthalmology, TUM University Hospital, Munich, Germany
[4]Department of Ophthalmology, University of Bonn, Bonn, Germany

Correspondence: Maximilian Pfau, Department of Ophthalmology, University of Basel, Mittlere Strasse 91, Basel CH-4031, Switzerland; Maximilian.Pfau@usb.ch.

JAWG and GA contributed equally to this study and should be considered joint first authors.
See the Appendix for the PROPXE Study Group.

Received: June 7, 2025
Accepted: October 11, 2025
Published: November 13, 2025

Citation: Giger JAW, Ansari G, Terry SF, Charbel Issa P, Pfau K, Pfau M. Measurement reliability and functional validity of Bruch's membrane calcification in pseudoxanthoma elasticum: PROPXE study report 2. *Invest Ophthalmol Vis Sci*. 2025;66(14):29. https://doi.org/10.1167/iovs.66.14.29

Purpose. The purpose of this study was to assess the inter-reader and inter-visit reliability of en face Bruch's membrane (BrM) calcification measurements in Pseudoxanthoma elasticum (PXE), investigate how the patient's age influences the BrM calcification extent, and evaluate the association between BrM calcification and delayed rod-mediated dark adaptation.

Methods. This prospective natural history study (PROPXE, ClinicalTrials.gov ID: NCT05662085) included 26 patients (14 women and 12 men; median age = 55 years, interquartile range = 43–59 years) diagnosed with PXE. Participants underwent comprehensive ophthalmic evaluations, including widefield infrared reflectance imaging (up to 83 degrees eccentricity) and dark adaptometry at retinal eccentricities of 8 degrees, 15 degrees, 30 degrees, and 46 degrees along the temporal retina. The primary outcomes were inter-visit and inter-reader reliability of the temporal inner peau d'orange boundary extent, its correlation with age, and its relationship with rod-intercept time (RIT) during dark adaptation.

Results. The temporal inner peau d'orange boundary showed excellent inter-reader and inter-visit reliability (inter-reader intraclass correlation coefficient [ICC] = 0.92 and inter-visit ICC = 0.95) and varied significantly with age (+4.35 deg/decade, P = 0.001). A greater temporal inner peau d'orange boundary extent was strongly associated with delayed rod-mediated dark adaptation at 8 degrees (+1.05 min/deg, P = 0.002) and 15 degrees (+0.91 min/deg, P = 0.001) eccentricities. A threshold effect was observed, with delayed dark adaptation at 8 degrees and 15 degrees eccentricity (from the fovea; i.e. 23 degrees and 30 degrees from the optic nerve head) manifesting once the temporal inner boundary exceeded 27.15 degrees and 32.56 degrees eccentricity (from the optic nerve head), respectively.

Conclusions. Patients with PXE demonstrate significant rod-mediated dark adaptation deficits correlating with the temporal inner peau d'orange boundary extent. These findings support the use of BrM calcification extent as an objective marker for disease severity, facilitating earlier therapeutic intervention than currently possible in PXE.

Keywords: pseudoxanthoma elasticum (PXE), grönblad-strandberg syndrome, light/dark adaptation, peau d'orange, angioid streaks

Pseudoxanthoma elasticum (PXE) is an inherited multisystem disorder primarily affecting elastic fiber-rich tissues in the vasculature, eyes, and skin.[1] It has an estimated prevalence of 1:56,000.[2] The disease arises due to biallelic mutations in the *ABCC6* gene, encoding an ATP-binding cassette transporter predominantly expressed in hepatocytes.[3,4] Loss-of-function mutations in ABCC6 markedly reduce plasma inorganic pyrophosphate levels, an essential inhibitor of ectopic calcification, leading to progressive calcification of elastic fibers across affected tissues.[5] In the eye, calcification of Bruch's membrane (BrM) is the primary lesion leading to secondary complications, such as angioid streaks, macular neovascularization (MNV), and macular atrophy.[1]

Quantification of PXE disease progression poses substantial challenges. Vascular-focused approaches, including whole-body low-dose computed tomography (CT) imaging or 18F-Sodium Fluoride positron emission tomography (PET)-CT imaging,[6,7] although comprehensive, lack sufficient resolution to quantify subtle progression sensitively and are expensive for routine clinical use. Previously, ocular clinical trial endpoints have predominantly focused on secondary complications, such as angioid streak length or onset of MNV, rather than directly measuring the progression of tissue calcification itself.[8] Likewise, the ocular component of the widely used Phenodex score primarily differentiates between the absence and presence of MNV as a secondary complication (rather than directly reflecting the underlying progression of BrM calcification) because cases without angioid streaks are rare.[9]

In principle, ophthalmic imaging could provide a promising avenue for directly quantifying BrM calcification, leveraging high-resolution visualization capabilities inherent to retinal imaging. The leading disease front, described as "peau d'orange,"[10–12] progresses centrifugally with age while encircling a central area of continuously calcified BrM (recently also termed "coquille d'œuf").[10,13] A recent quantitative study showed that the temporal outer boundary of peau d'orange is relatively stable, whereas the temporal inner boundary progresses centrifugally with age, resulting in thinning of the peau d'orange and expansion of the area of continuously calcified BrM.[14] However, the measurement characteristics of delineating BrM calcification (inter-reader and inter-visit reliability, and inter-eye concordance) remain unknown. Moreover, the functional impact of peau d'orange and continuously calcified BrM is not yet established. The first report of the PROPXE study demonstrated using multifocal dark adaptometry that delayed cone- and rod-mediated dark adaptation follows – on average – the spatial topography of calcified BrM.[15] Thus, in addition to measurement characteristics, linking BrM calcification at the individual patient level to dysfunction remains a critical need for establishing the extent of calcified BrM as a patient-relevant outcome measure.

The aims of this study are fourfold. First, we aim to assess the inter-reader reliability for quantifying the extent of peau d'orange and the region of continuously calcified BrM. Second, we evaluate the inter-visit reliability of these imaging biomarkers. Third, we substantiate the presumed age-related progression of BrM calcification as a foundational requirement for longitudinal measurement feasibility. Last, we seek to establish the patient relevance of these imaging biomarkers by determining their associations with measures of visual function, thus clarifying their potential role as meaningful endpoints in future clinical trials.

METHODS

The study protocol has been described previously in detail (prospective natural history investigation titled "Progression Rate of Pseudoxanthoma Elasticum-associated Choroidal and Retinal Degeneration," [PROPXE], ClinicalTrials.gov Identifier: NCT05662085).[15] Ethical approval was granted by the responsible human research ethics committee (EKNZ), and the study adhered strictly to the principles outlined in the Declaration of Helsinki. Written informed consent was obtained from every participant.

Study Design

The study included adult patients diagnosed with PXE according to the criteria defined by Plomp and coworkers.[16] The best-corrected visual acuity (BCVA) in the study eye was required to be $\leq$1.0 logMAR or better. Exclusion criteria encompassed inability to provide informed consent, severe claustrophobia, previous ocular surgeries other than allowed interventions (anti-VEGF injections, cataract surgery, YAG laser capsulotomy, or laser retinopexy), concurrent ophthalmic conditions in the study eye that might independently affect visual acuity, as judged by the investigator, and planned major surgeries or events potentially impeding follow-up evaluations.

The primary selection for the study eye favored eyes without a medical history of exudative MNV. If both eyes shared a similar history (either presence or absence of exudative MNV), the eye with better BCVA was chosen. If BCVA was identical in both eyes, the right eye was selected.

The study protocol comprised an initial baseline visit, a retest session at 2 months, and subsequent follow-up visits after 1 year and 2 years. The current report details findings from the baseline and month 2 retest visits.

Examinations

Participants underwent extensive ophthalmological assessments, including BCVA measurement using the quantitative visual acuity (qVA) protocol on the Manifold platform (Adaptive Sensory Technology, Lübeck, Germany), alongside quick contrast sensitivity function (qCSF) testing conducted on the same platform.

Standardized multimodal imaging techniques were systematically applied. Spectral-domain optical coherence tomography (SD-OCT) imaging was performed, acquiring macular scans covering 30 degrees × 25 degrees with 121 B-scans (automatically averaged over 25 scans per image), as well as Bruch's membrane opening (BMO) scans using the Heidelberg Spectralis OCT2 (Heidelberg Engineering, Heidelberg, Germany). Additionally, 55 degrees fundus autofluorescence and infrared (IR) reflectance imaging were captured. The 55 degrees IR reflectance images were acquired centrally, as well as peripherally, using the eight eccentric preset fixation targets of the Spectralis OCT2 device (total of 9 fields). The fields extended jointly to 82.5 degrees eccentricity from the fovea in all directions.

In addition, patients underwent multifocal dark adaptometry at each visit using the MonCvONE device (Metrovision, Perenchies, France). The protocol used a full-field bleach (634 photopic cd/m^2, equivalent to 946 scotopic cd/m^2) lasting 5 minutes (59% rhodopsin bleaching). Cyan and red Goldmann V-sized stimuli (peak wavelengths 500 nm and 647 nm, stimulus duration 200 ms, initial luminance 0.318 phot. cd/m^2 [–3 LogUnits]) were presented at retinal loci 8 degrees, 15 degrees, 30 degrees, and 46 degrees temporal to fixation (i.e. nasal visual field). Testing continued for up to 60 minutes or ended earlier if steady-state rod thresholds were reached at all 4 loci. The rod-intercept time (RIT) was defined as the time to reach the criterion threshold of -5 LogUnits (0.00318 phot. cd/m^2, i.e. approximately 1 LogUnit below the normal cone threshold).[15,17]

Image Processing

A wide-field imaging montage was generated automatically using a custom-developed ImageJ software plugin. Briefly, the Scale Invariant Feature Transform (SIFT) algorithm identified corresponding landmarks between the central image and four peripheral images captured along the main axes (superior, inferior, temporal, and nasal). These peripheral images were then registered to the central image using

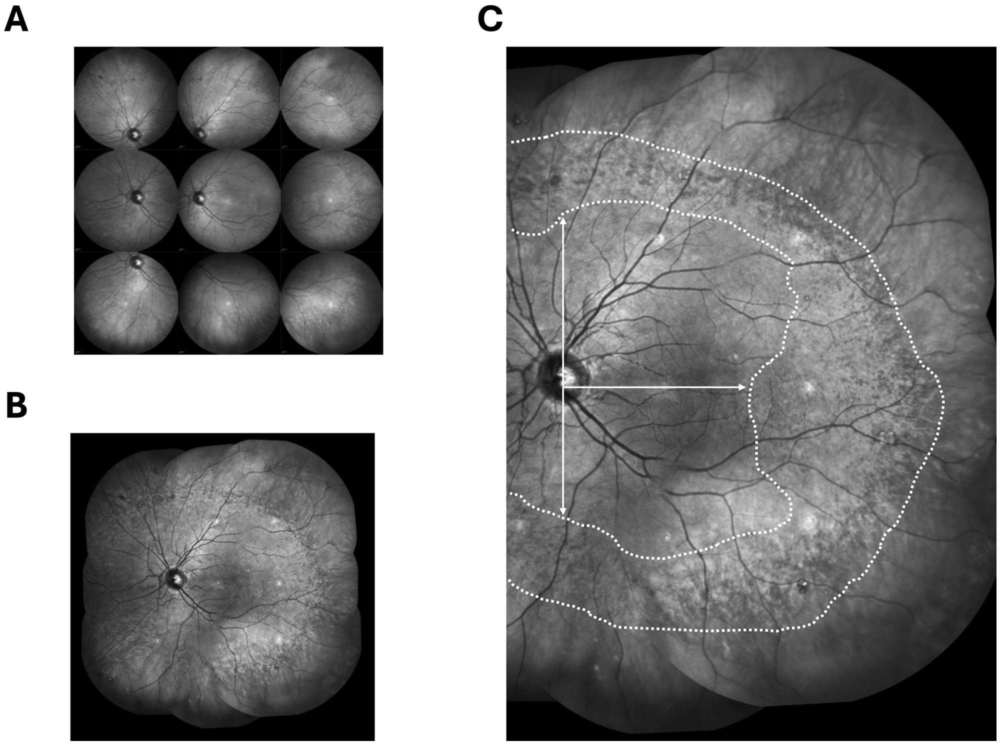

Figure 1. Wide-field infrared (IR) reflectance imaging montage and image annotation. The 9-field 55 degrees IR images were registered semi-automatically to obtain a wide-field IR montage (**A**, **B**). Subsequently, three readers independently annotated the peau d'orange outer and inner boundaries (**C**). Last, the temporal, superior, and inferior boundary extents were extracted automatically. The temporal meridian was defined as the horizontal line starting at the level of the optic disc center and going through the fovea. The vertical superior and inferior meridians had the exact same origin (i.e. vertical position based on the vertical position of the foveal center and horizontal position based on the horizontal center of the optic disc).

an affine transformation. Subsequently, the remaining four peripheral fields underwent the same registration process to the newly formed composite image. If automatic registration was unsuccessful, corresponding retinal landmarks were manually selected to ensure accurate alignment. The foveal position was identified on the SD-OCT scan and registered to the wide-field montage.

Image Grading

Three independent readers evaluated all images. As part of the standardized grading protocol, each reader initially used the oval selection tool in ImageJ software to outline the approximate inner and outer boundaries of the peau d'orange area. These regions were saved as reference regions of interest for orientation. In the next step, the precise boundaries of the peau d'orange were delineated using the freehand selection tool, allowing readers to follow natural contour variations, including concavities and convexities. Following an initial quality control check, the grading task was repeated to ensure consistent adherence to anatomic details. Specifically, readers were requested to follow, if present, the concavity of the temporal peau d'orange boundary related to the "temporal spared island" in PXE (cf., fig. 2 in PC Issa et al. 2010).[18] To further distinguish peau d'orange from subretinal drusenoid deposits (SDDs), annotators applied multiple criteria. Peau d'orange typically appears as a fine, isoreflective dotted pattern (relative to the unaffected retina) within an area of increased reflectance, whereas SDDs present as round-to-oval or ribbon-like hyporeflective formations (cf., Supplementary Fig. S1B).[19] The extent of angioid streaks also served as a landmark, as the longest streaks generally terminate at or near the peau d'orange inner boundary (Supplementary Fig. S1C).[1] Finally, natural history was taken into account: SDDa have been reported to occur only in eyes where the temporal extent of the peau d'orange inner boundary is ≥19 degrees (5.6 mm) from the optic nerve head.[19]

As shown in Figure 1, an ImageJ software plugin was used to extract the boundary extents measured along the horizontal temporal meridian (defined by the horizontal axis starting at the eccentricity of the optic disc center and going through the fovea) as well as along the superior and inferior meridians. The nasal side was not analyzed, as peau d'orange boundaries frequently extended beyond the region that could be reliably visualized. Although annotations were performed in 2D, we elected to report data along predefined meridians because image quality and annotation reliability varied across meridians. The superior and inferior meridians were often affected by shadowing from the upper or lower lids, leading to reduced peripheral contrast in some patients, whereas the temporal meridian typically offered the most consistent and highest-contrast visualization.

Statistical Analyses

The inter-reader reliability was assessed using Bland-Altman analysis and reliability statistics (coefficient of variation, standard error of measurement, and intraclass correlation coefficient [ICC; 2-way random, agreement]) with the *R* software package *SimplyAgree*.[20] Subsequently, the measurements from the readers were averaged to assess the inter-visit reliability and the inter-eye concordance.

For the association analyses, we fitted a series of linear mixed-effects models with *lme4*.[21] These models included data from both study and non-study eyes, incorporating a random effects structure with eye nested within participant. First, we assessed the association between age and the six peau d'orange boundary extents (defined as the inner and outer boundaries along the temporal, superior, and inferior meridians) to estimate the ocular disease progression rate.

In separate models, we examined the relationship between RIT at four eccentricities (8 degrees, 15 degrees, 30 degrees, and 46 degrees) and peau d'orange boundary extents, using baseline and retest-visit data from study eyes only. In these models, patient ID was included as a random effect, and age was included as a covariate (as age acts as a classical confounder, affecting both peau d'orange boundary extents and RIT).

To account for multiple comparisons across all tests, a Bonferroni-corrected threshold of $P < 0.0017$ (0.05/30). This threshold was derived from 30 total hypothesis tests: 6 tests assessing the effect of age on the 6 boundaries (3 inner and 3 outer boundaries), and 24 tests evaluating the association of the same 6 boundary measures with RIT at 4 eccentricities ($6 \times 4 = 24$).

In addition, we performed a secondary analysis using the Benjamini–Hochberg procedure to control the false discovery rate (FDR) for the family of tests evaluating the association between peau d'orange boundary extent and RIT. The FDR adjustment was applied only to the primary effects of interest (boundary extent), whereas covariates such as age were included for adjustment but not subjected to multiple-testing correction.

Last, we fitted nonlinear mixed models with a step-function to describe the association between the temporal outer peau d'orange boundary extent and RIT at 8 degrees and 15 degrees more accurately using *brms* (cf. Supplementary Methods).[22]

RESULTS

Cohort

This analysis included all 26 individuals with genetically confirmed PXE described in the baseline report, including 14 women (53.8%) and 12 men (46.2%). The participants had a median age of 55 years (interquartile range = 43 to 59 years), with ages spanning from 25.7 to 66.9 years.

In the designated study eye, 12 participants (46.2%) had no history of exudative MNV, whereas 14 participants (53.8%) had current or prior treatment for exudative MNV. Median BCVA in the study eye was −0.07 logMAR (interquartile range = −0.07 to 0.11), which corresponds to a Snellen equivalent of approximately 20/17 (range = 20/17 to 20/26).

The average (median) interval between the baseline and the retest visits was 1.9 months.

Inter-Reader and Inter-Visit Reliability

Assessment of inter-reader reliability for peau d'orange boundary delineation revealed consistent patterns across both the baseline and retest visits (Figs. 2A–C; Supplementary Table S1). At baseline, the standard error of measurement was similar across all inner boundaries (temporal inner estimate, 95% confidence interval [95% CI] = 2.68 degrees [95% CI = 2.11–3.17]; superior inner = 2.35 degrees [95% CI = 1.86–2.87]; inferior inner = 2.93 degrees [95% CI = 2.32–3.47]). But the temporal inner boundary exhibited the lowest ICC at both visits (ICC = 0.92 [95% CI = 0.89–0.95] at V1; ICC = 0.82 [95% CI = 0.74–0.88] at V2), given the greatest reliability in relation to the overall variability in boundary extent (see Supplementary Table S1). Figure 2 shows the Bland-Altman plots for between-reader reliability in delineating the temporal inner peau d'orange boundary. The outer boundaries consistently demonstrated relatively small (absolute) standard errors of measurement too, but lower ICCs, particularly inferior and superior (ranging from 0.32 to 0.61; see Supplementary Table S1).

The inter-visit reliability (with averaging the data from the 3 readers) was excellent overall (Supplementary Table S2). For the temporal inner peau d'orange boundary, the standard error of measurement was 1.97 degrees [95% CI = 1.57–2.29] with an ICC of 0.95 [95% CI = 0.93–0.97].

Between-Eye Concordance

Overall, there was a considerable concordance between the right eye and left eye peau d'orange boundary extents (see Fig. 3; Supplementary Table S3). But the between-eye differences exceeded the inter-visit differences. For example, the standard error of measurement between the right and left eyes was 3.52 degrees [95% CI = 2.89–4.06] for the temporal inner peau d'orange boundary.

Association of BrM Calcification With Age

Linear mixed-effects model analysis revealed a significant association between age and the extent of the temporal inner peau d'orange boundary, with an estimated increase of +4.35 deg/decade (95% CI = 1.81–6.89, $P = 0.001$). Age alone explained 23% of the variability in temporal inner peau d'orange boundary extent (marginal R^2). In contrast, no association was evident between age and the temporal outer peau d'orange boundary (estimate = −0.28 deg/decade, 95% CI = −1.19 to 0.64, $P = 0.556$).

Along the superior and inferior meridians, age was associated with neither the extent of the inner nor outer peau d'orange boundaries (Supplementary Table S4). Notably, the current data recapitulated previously published estimates of temporal inner and outer peau d'orange boundary extent (see Supplementary Fig. S1).

Association of BrM Calcification With Delayed Dark-Adaptation

To examine whether the spatial extent of the temporal inner peau d'orange boundary is associated with impaired rod-mediated dark adaptation, a linear mixed-effects model was fitted with RIT at 15 degrees eccentricity as the dependent variable and temporal inner peau d'orange boundary extent and age as fixed effects (Fig. 4; Supplementary Fig. S2). These fixed effects alone accounted for a substantial proportion of variance (marginal $R^2 = 0.341$; Supplementary Table S5). The temporal inner peau d'orange boundary extent was associated with delayed RIT at 15 degrees with

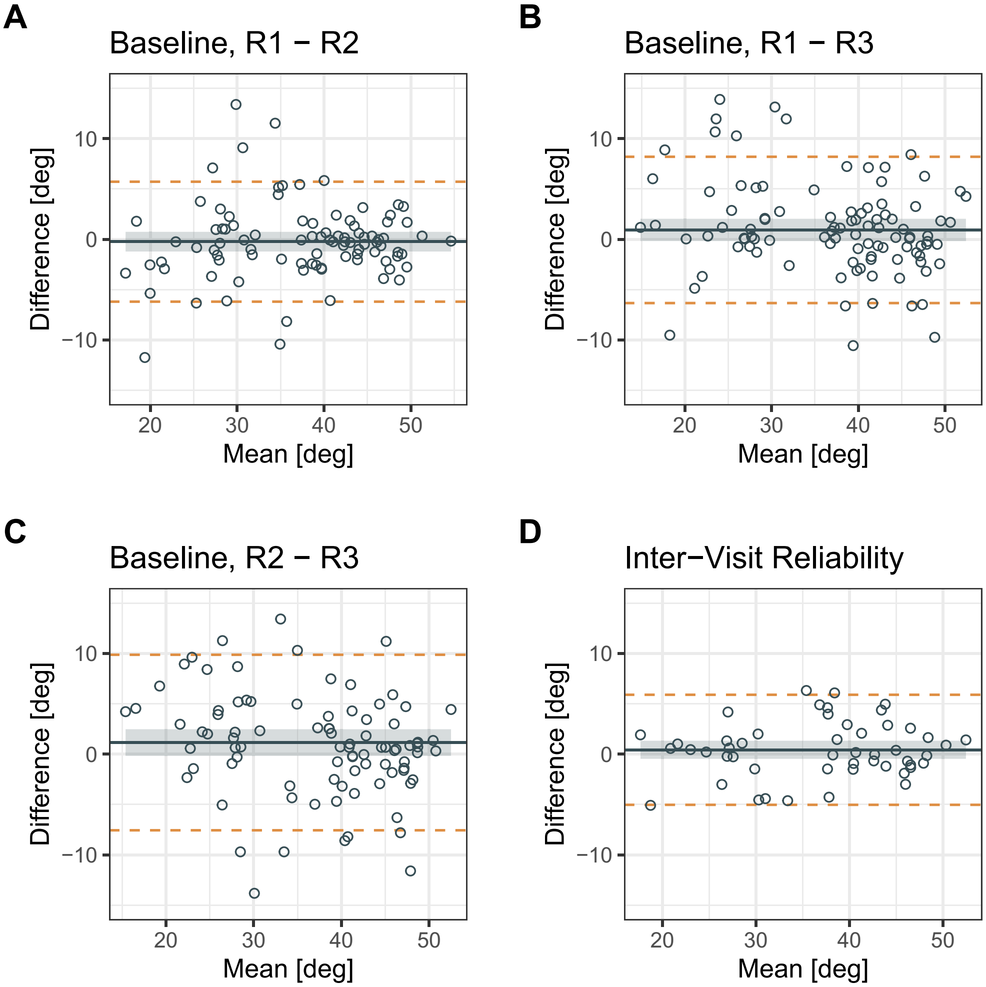

Figure 2. **Inter-reader reliability and inter-visit reliability for the temporal inner peau d'orange boundary extent.** (**A, B, C**) The Bland-Altman plots show the inter-reader reliability, incorporating data from both the baseline and retest visits. The *solid gray line* and *ribbon* indicate the bias and 95% confidence interval, whereas the *orange dashed lines* represent the 95% limits of agreement. (**D**) The last Bland-Altman plot displays the inter-visit reliability (including averaging of the grader's individual measurements).

+0.91 min/deg (95% CI = 0.37–1.44, $P = 0.001$), whereas age did not contribute significantly to the prediction of RIT (+0.83 min/decade, 95% CI = −3.76 to 5.41, $P = 0.719$).

Using the Benjamini–Hochberg procedure, the temporal inner peau d'orange boundary extent was also significantly associated with delayed RIT at 8 degrees. In contrast, the inner boundary extents along the superior and inferior meridians were not significantly associated with RIT under either the Bonferroni or Benjamini–Hochberg correction. However, the effect estimates for the association between the superior inner peau d'orange boundary extent and RIT at 8 degrees and 15 degrees were similar (see Supplementary Tables S5–S8 for the Benjamini–Hochberg procedure).

Sensitivity analyses revealed that the association between peau d'orange boundary extent and RIT was stronger in the younger half of the cohort than in the older patients, given the RIT ceiling of 60 minutes (Supplementary Table S9).

Because the relationship between the temporal inner peau d'orange boundary extent and RIT at 8 degrees or 15 degrees followed a hockey stick, we fitted a Bayesian nonlinear mixed model to these data. Delays in RIT at 8 degrees and 15 degrees (i.e. at 23 degrees and 30 degrees from the optic nerve head) were estimated to occur once the temporal inner peau d'orange boundary extended from the optic nerve head by more than 27.15 degrees (95% Bayesian credible interval = 17.06, 33.09) and 32.56 degrees (95% Bayesian credible interval = 22.64, 40.56), respectively (Supplementary Table S10). Figure 5 shows two exemplary patients.

Discussion

A major clinical challenge in PXE is accurately quantifying the progression of calcification. To date, ophthalmic assessments focus predominantly on secondary complications, such as angioid streak length or MNV,[14,23] rather than directly measuring the calcification process itself. This approach, however, measures probabilistic events and does not fully capture the underlying pathophysiology or the continuous disease progression. In the present study, we established essential measurement properties required for quantifying the extent of BrM calcification. Specifically, we demonstrated good inter-reader and inter-visit reliability, as well as substantial inter-eye concordance in peau d'orange boundaries delineated using wide-field IR imaging.

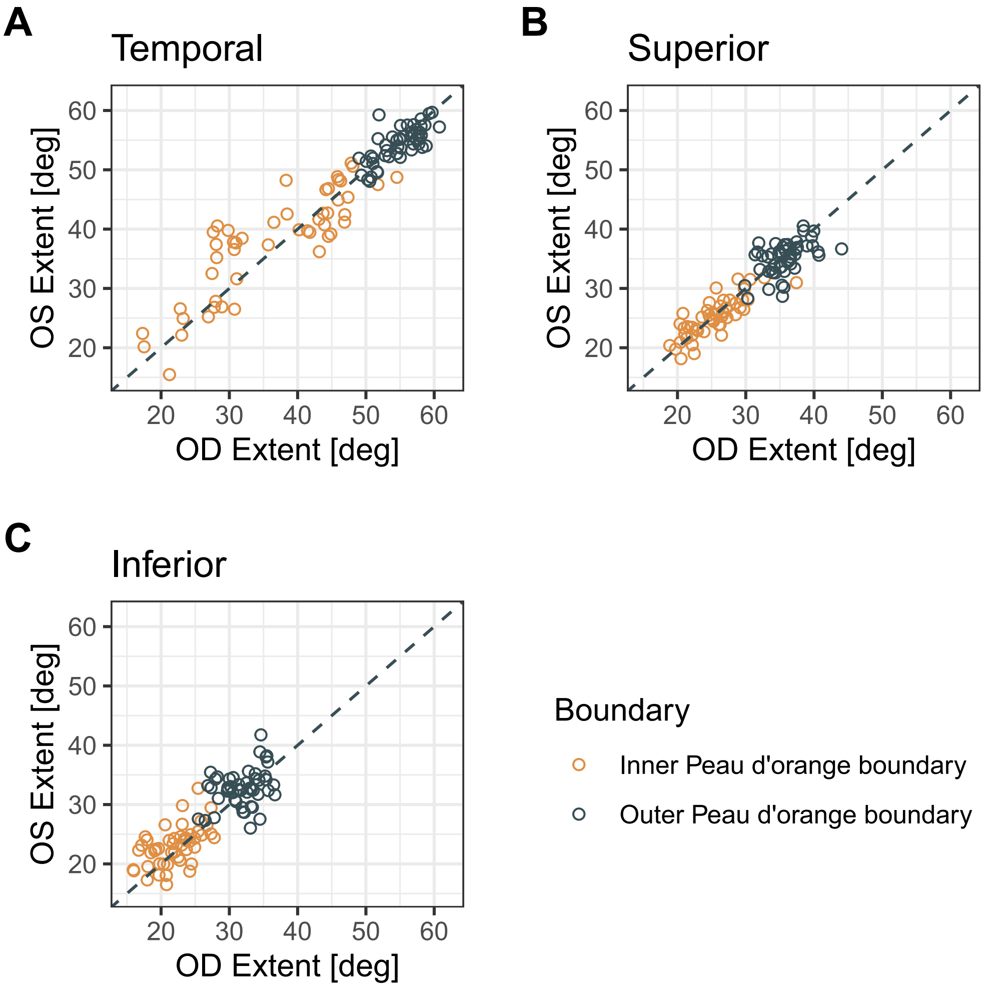

Figure 3. Inter-eye concordance for the peau d'orange boundary extents. The panels display the scatter plots for the peau d'orange boundary extents along the temporal (**A**), superior (**B**), and inferior (**C**) meridians for the right and left eyes. The *gray circles* indicate outer boundary measurements, whereas the *orange circles* represent inner boundary measurements.

Furthermore, our data support evaluating the age-associated centrifugal expansion of the inner peau d'orange boundary as an indicator of disease progression over time. Critically, we demonstrated a significant functional relevance of the temporal inner peau d'orange boundary extent by showing its association with delayed rod-mediated dark adaptation.

Regarding measurement properties of BrM calcification, our findings highlight that assessing peau d'orange is feasible but methodologically challenging. The absolute inter-reader and inter-visit reliability across all three meridians was similar, but the ICC varied markedly among meridians and boundaries. The ICC, which represents the ratio of variance of interest (true differences between patients) to the total variance (true differences plus measurement error), was notably higher for the temporal inner peau d'orange boundary. This likely reflects both greater genuine inter-individual variance along the horizontal meridian – consistent with the oval shape of BrM calcification in PXE (cf. spread in Fig. 2A versus Figs. 2B, 2C) – and partial lid shadowing artifacts frequently reducing the image quality along the superior and inferior meridians. Practically, the temporal inner peau d'orange boundary therefore provides the best signal-to-noise ratio for association studies with age, systemic measures of disease severity, or visual function. Biologically, the associations between inner peau d'orange boundary extent and function are expected to be similar across meridians; the associations for the superior and inferior inner peau d'orange boundary extent with RIT are most parsimoniously explained by lower measurement reliability rather than by true absence of effect.

Qualitative observation suggested that boundary delineation was complicated by subretinal drusenoid deposits,[19] which may mimic peau d'orange appearance, and the phenomenon known as the "temporal spared island,"[18] which creates complex grading scenarios. Additionally, an often-thinned choroid in PXE,[24–26] in conjunction with low choroidal pigmentation in lighter-skinned patients, can result in a diminished contrast in IR imaging, exacerbating the difficulty of delineating the peau d'orange boundaries. Thus, contrast-rich measures of disease severity should be explored in future studies. For example, the outer hypo-fluorescent speckled pattern visible in late-phase indocyanine angiography has been previously reported to align close to the peau d'orange inner boundary,[18] but data on the association with age or change-over-time are lacking.

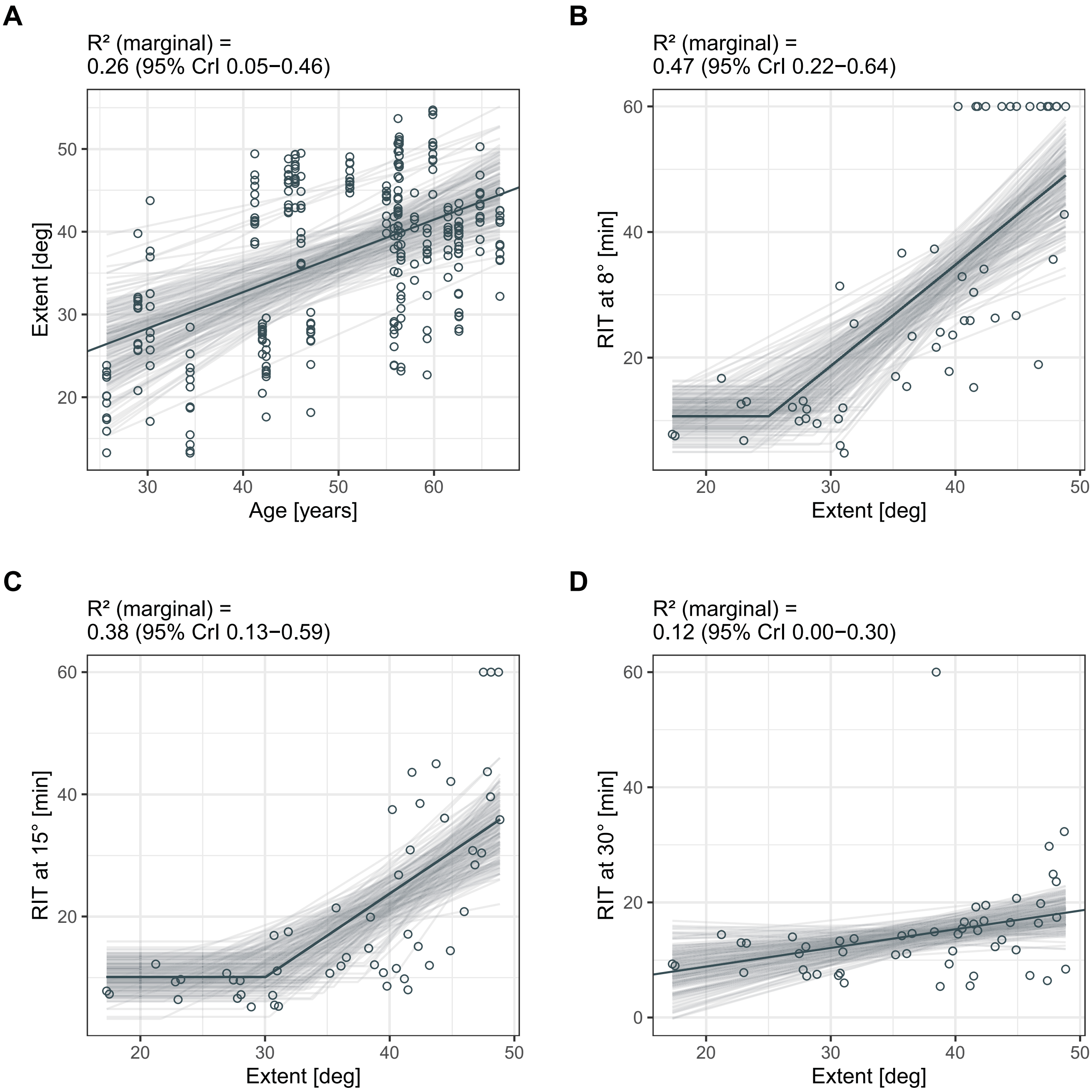

FIGURE 4. **Association between age and the temporal inner peau d'orange boundary and relationship to dark adaptation.** (**A**) The first panel shows the association between age and the extent of the temporal inner peau d'orange boundary, with data points from both eyes and visits plotted. (**B, C, D**) The panels **B** to **D** illustrate the relationship between the temporal inner boundary and rod-intercept time (RIT), a measure of dark adaptation, at 8 degrees, 15 degrees, and 30 degrees eccentricity. Regression lines were derived from Bayesian linear or nonlinear mixed models, with step functions applied where appropriate. Thin lines represent posterior draws of the expected value, visualizing the range of plausible fits under the model. Marginal R^2 values (with 95% credible intervals [CrI]) indicate the proportion of variance explained by the fixed effects alone. (**B–D**) Are shown without age adjustment, illustrating the unadjusted association between peau d'orange extent and RIT. For reference, the extent of peau d'orange was defined as eccentricity from the optic nerve head, whereas RIT was defined relative to the fovea (i.e. 15 degrees temporal to the optic nerve head). Therefore, the observed breakpoints in panels **C** and **D** align very closely with the locations at which RIT was measured.

We further substantiated a clear association between age and the temporal inner peau d'orange boundary extent, consistent with previous reports.[14] Our observed rate of 4.4 degrees per decade (approximately 1.3 mm per decade in an emmetropic eye) is of similar magnitude as reported by one previous study (6.2 degrees per decade, see Supplementary Fig. S1).[14] The slight difference is likely linked to the difference in age of the patient populations, with patients >50 years of age in our cohort that are likely close to the ceiling in terms of temporal inner peau d'orange boundary extent (ceiling expected in the range of 50 degrees to 60 degrees based on our temporal outer peau d'orange data). These

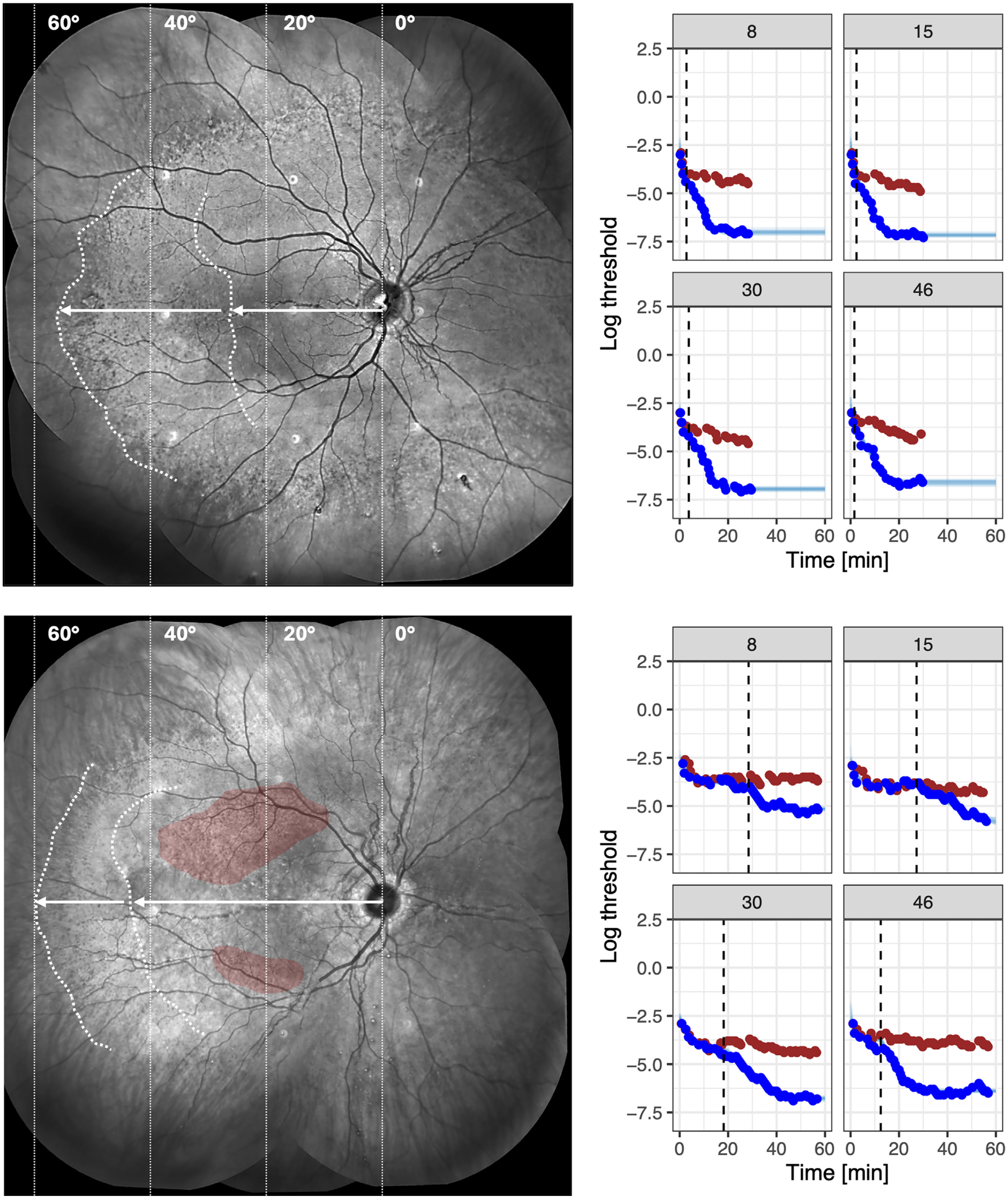

Figure 5. **Patient examples.** The *upper row* shows a patient with a temporal inner peau d'orange boundary within the central 30 degrees. The rate of dark adaptation at all loci is within normal limits (panels for 8 degrees, 15 degrees, 30 degrees, and 46 degrees eccentricity, *blue dots* for the 500 nm stimulus, *red dots* for the 647 nm stimulus, and *vertical dashed lines* denoting the cone-rod-break). The *lower row* shows a patient with proximity of the inner and outer peau d'orange boundary. Notably, the dark adaptation at 15 degrees eccentricity is markedly delayed. The *red overlays* highlight areas with subretinal drusenoid deposits (SDDs), which can be mistaken for peau d'orange.

data underscore a relatively slow progression compared with lesions in other types of inherited retinal diseases. For example, the centrifugal progression of flecks in Stargardt disease was shown to be three to four times faster (1.1 degrees to 1.6 degrees per year).[27]

Importantly, our data established a direct link between the structural biomarker – temporal inner peau d'orange boundary extent – and delayed rod-mediated dark adaptation. In analogy to other diseases associated with deposits at the level of BrM, such as Sorsby fundus dystrophy,[28,29] late-onset retinal degeneration,[30] and age-related macular degeneration,[17,31–34] we previously hypothesized that BrM calcification in PXE hinders the interchange between the choroid and retinal pigment epithelium, slowing the visual cycle.[15,35] However, the precise link between the extent of BrM calcification and delayed dark adaptation on the individual patient level was lacking previously. This link now documents the functional relevance of BrM calcification as a prerequisite for its application as an endpoint for future clinical trials. At the same time, the strength of association was modest: the temporal inner boundary accounted for approximately ⅓ of the variance in dark adaptation, leaving a considerable fraction unexplained. This may reflect variability in measurement, both for BrM calcification and for the outcome itself (RIT), as well as potential confounding influences such as subretinal drusenoid deposits or vitamin A intake. Priorities going forward include minimizing measurement variability, clarifying and adjusting for potential confounders, and extending validation to establish whether BrM calcification is also a surrogate for other clinically relevant outcomes, such as cardiovascular events. Complementary to our findings, previous research indicated that the extent of calcification (assessed by angioid streak length) also correlates with central visual impairment resulting from macular neovascularization or atrophy.[36]

At the same time, the strength of association was modest: the temporal inner boundary accounted for approximately ⅓ of the variance in dark adaptation, leaving the majority unexplained.

Limitations of the current study should be considered. First, our cohort size, although representative for rare diseases such as PXE, is relatively small. Nevertheless, robust associations between structural measures and visual function were identified, given the application of advanced visual function testing, including multifocal dark adaptometry. Second, differentiation between SDD and peau d'orange was based on imaging characteristics in IR reflectance and heuristic criteria (see Supplementary Fig. S1); whereas a multimodal imaging approach would be preferable. Importantly, any misclassification of SDD as peau d'orange would be expected to attenuate, rather than artificially strengthen, the observed associations. Additionally, the study's short-term retest design does not fully capture long-term variability or progression dynamics over extended periods. Future longitudinal studies, ideally using fundus-tracked dark adaptometry,[37] are required to definitively establish causal relationships and validate the temporal inner peau d'orange boundary as a biomarker of visual function in PXE.

In summary, our study demonstrates the feasibility of quantifying en face BrM calcification progression using wide-field IR imaging montages in PXE, despite methodological complexities. The temporal inner peau d'orange boundary notably correlates with age, reflecting disease progression. Moreover, this biomarker strongly associates with rod-mediated dark adaptation delays, reinforcing its functional relevance. Consequently, quantifying the temporal inner peau d'orange boundary is a candidate clinical trial endpoint, providing a patient-relevant measure of disease progression and therapeutic efficacy in PXE.

Acknowledgments

Supported by the BrightFocus Foundation (grant M2024009N [MP]), and by the German Research Foundation (532367710 [KP]).

Disclosure: **J.A.W. Giger**, None; **G. Ansari**, iCare (R); **S.F. Terry**, Daiichi Sankyo (C); **P. Charbel Issa**, Heidelberg Engineering (F), Roche (R), Novartis (R), Bayer (R), and Apellis (R); **K. Pfau**, Daichii Sankyo (C), Inozyme (F), Heidelberg Engineering (R), Bayer (R), and Roche (R); **M. Pfau**, iCare (F), Inozyme (F)

References

1. Pfau K, Lengyel I, Ossewaarde-van Norel J, et al. Pseudoxanthoma elasticum – genetics, pathophysiology, and clinical presentation. *Prog Retin Eye Res*. 2024;102:101274.
2. Kranenburg G, Baas AF, de Jong PA, et al. The prevalence of pseudoxanthoma elasticum: revised estimations based on genotyping in a high vascular risk cohort. *Eur J Med Genet*. 2019;62(2):90–92.
3. Le Saux O, Beck K, Sachsinger C, et al. A spectrum of ABCC6 mutations is responsible for pseudoxanthoma elasticum. *Am J Hum Genet*. 2001;69(4):749–764.
4. Bergen AA, Plomp AS, Schuurman EJ, et al. Mutations in ABCC6 cause pseudoxanthoma elasticum. *Nat Genet*. 2000;25(2):228–231.
5. Jansen RS, Küçükosmanoglu A, de Haas M, et al. ABCC6 prevents ectopic mineralization seen in pseudoxanthoma elasticum by inducing cellular nucleotide release. *Proc Natl Acad Sci USA*. 2013;110(50):20206–20211.
6. Omarjee L, Mention PJ, Janin A, et al. Assessment of inflammation and calcification in pseudoxanthoma elasticum arteries and skin with 18F-FluroDeoxyGlucose and 18F-Sodium Fluoride positron emission tomography/computed tomography imaging: the GOCAPXE Trial. *J Clin Med*. 2020;9(11):3448.
7. Harmsen IM, Visseren FLJ, Kok M, de Jong PA, Spiering W. Arterial calcification volume is associated with a higher risk of cardiovascular events in pseudoxanthoma elasticum. *Atherosclerosis*. 2025;400:119051.
8. Kranenburg G, de Jong PA, Bartstra JW, et al. Etidronate for prevention of ectopic mineralization in patients with pseudoxanthoma elasticum. *J Am Coll Cardiol*. 2018;71(10):1117–1126.
9. Pfendner EG, Vanakker OM, Terry SF, et al. Mutation detection in the ABCC6 gene and genotype-phenotype analysis in a large international case series affected by pseudoxanthoma elasticum. *J Med Genet*. 2007;44(10):621–628.
10. Grönblad EE. Der Zusammenhang zwischen »Angioid streaks« und Pseudoxanthoma elasticum. *Acta Ophthalmol*. 1932;10(S1):66–97.
11. Grönblad EE. Color photographs of angioid streaks in the late stages. *Acta Ophthalmol*. 1958;36(3):472–474.
12. Smith JL, Gass JDM, Justice J. Fluorescein fundus photography of angioid streaks. *Br J Ophthalmol*. 1964;48(10):517–521.
13. Spaide RF. Peau d'orange and angioid streaks: manifestations of Bruch membrane pathology. *Retina*. 2015;35(3):392–397.
14. Risseeuw S, van Leeuwen R, Imhof SM, Spiering W, Norel JO van. The natural history of Bruch's membrane calci-

fication in pseudoxanthoma elasticum. *Ophthalmol Sci.* 2021;1(1):100001.

15. Pfau K, Ansari G, Michels S, et al. Topography of slowed dark adaptation in pseudoxanthoma elasticum: PROPXE Study Report 1. *Invest Ophthalmol Vis Sci.* 2025;66(2):17.
16. Plomp AS, Toonstra J, Bergen AA, van Dijk MR, de Jong PT. Proposal for updating the pseudoxanthoma elasticum classification system and a review of the clinical findings. *Am J Med Genet A.* 2010;152A(4):1049–1058.
17. Hess K, de Silva T, Grisso P, et al. Evaluation of cone- and rod-mediated parameters in dark adaptation testing as outcome measures in age-related macular degeneration. *Ophthalmol Retina.* 2022;6(12):1173–1184.
18. Charbel Issa P, Finger RP, Götting C, Hendig D, Holz FG, Scholl HPN. Centrifugal fundus abnormalities in pseudoxanthoma elasticum. *Ophthalmology.* 2010;117(7):1406–1414.
19. Gliem M, Hendig D, Finger RP, Holz FG, Charbel Issa P. Reticular pseudodrusen associated with a diseased Bruch membrane in pseudoxanthoma elasticum. *JAMA Ophthalmol.* 2015;133(5):581–588.
20. Caldwell AR. SimplyAgree: an R package and jamovi module for simplifying agreement and reliability analyses. *J Open Source Softw.* 2022;7(71):4148.
21. Bates D, Mächler M, Bolker BM, Walker SC. Fitting linear mixed-effects models using lme4. *J Stat Softw.* 2015;67(1):1–48.
22. Bürkner PC. brms: an R package for Bayesian multilevel models using stan. *J Stat Softw.* 2017;80(1):1–28.
23. Kranenburg G, de Jong PA, Bartstra JW, et al. Etidronate for prevention of ectopic mineralization in patients with pseudoxanthoma elasticum. *J Am Coll Cardiol.* 2018;71(10):1117–1126.
24. Gliem M, Fimmers R, Müller PL, et al. Choroidal changes associated with Bruch membrane pathology in pseudoxanthoma elasticum. *Am J Ophthalmol.* 2014;158(1):198–207.e3.
25. Risseeuw S, Bartstra J, Ossewaarde-van Norel J, et al. Is arterial stiffness in the carotid artery associated with choroidal thinning in patients with pseudoxanthoma elasticum or controls? *Acta Ophthalmol.* 2020;98(5):492–499.
26. Loewinger AS, Pfau M, Herrmann P, Holz FG, Pfau K. Choriocapillaris flow signal impairment in patients with pseudoxanthoma elasticum. *Invest Ophthalmol Vis Sci.* 2023;64(2):21.
27. Cideciyan A V., Swider M, Schwartz SB, Stone EM, Jacobson SG. Predicting progression of ABCA4-associated retinal degenerations based on longitudinal measurements of the leading disease front. *Invest Ophthalmol Vis Sci.* 2015;56(10):5946–5955.
28. Jacobson SG, Cideciyan AV, Regunath G, et al. Night blindness in Sorsby's fundus dystrophy reversed by vitamin A. *Nat Genet.* 1995;11(1):27–32.
29. Raming K, Gliem M, Charbel Issa P, et al. Visual dysfunction and structural correlates in Sorsby fundus dystrophy. *Am J Ophthalmol.* 2022;234:274–284.
30. Jacobson SG, Cideciyan A V, Wright E, Wright AF. Phenotypic marker for early disease detection in dominant late-onset retinal degeneration. *Invest Ophthalmol Vis Sci.* 2001;42(8):1882–1890.
31. Steinmetz RL, Haimovici R, Jubb C, Fitzke FW, Bird AC. Symptomatic abnormalities of dark adaptation in patients with age-related Bruch's membrane change. *Br J Ophthalmol.* 1993;77(9):549–554.
32. Owsley C, McGwin G, Clark ME, et al. Delayed rod-mediated dark adaptation is a functional biomarker for incident early age-related macular degeneration. *Ophthalmology.* 2016;123(2):344–351.
33. Flynn OJ, Cukras CA, Jeffrey BG. Characterization of rod function phenotypes across a range of age-related macular degeneration severities and subretinal drusenoid deposits. *Invest Ophthalmol Vis Sci.* 2018;59(6):2411–2421.
34. Fraser RG, Tan R, Ayton LN, Caruso E, Guymer RH, Luu CD. Assessment of retinotopic rod photoreceptor function using a dark-adapted chromatic perimeter in intermediate age-related macular degeneration. *Invest Ophthalmol Vis Sci.* 2016;57(13):5436–5442.
35. Hess K, Gliem M, Birtel J, et al. Impaired dark adaptation associated with a diseased Bruch membrane in pseudoxanthoma elasticum. *Retina.* 2020;40:1988–1995.
36. Risseeuw S, Ossewaarde-van Norel J, van Buchem C, Spiering W, Imhof SM, van Leeuwen R. The extent of angioid streaks correlates with macular degeneration in pseudoxanthoma elasticum. *Am J Ophthalmol.* 2020;220:82–90.
37. Oertli JM, Pfau K, Scholl HPN, Jeffrey BG, Pfau M. Establishing fully-automated fundus-controlled dark adaptometry: a validation and retest-reliability study. *Transl Vis Sci Technol.* 2023;12(12):18.

APPENDIX: THE PROPXE STUDY GROUP

Stephan Michels[1,2], Chantal Dysli[3], Sandra Liakopoulos[4,5], Jana Burghaus-Zhang[6], Mayss Al-Sheikh[7], Justus G. Garweg[3,8], Mathieu Quinodoz[9–11], Karolina Kaminska[9,10], Francesca Cancellieri[9,10], and Carlo Rivolta[9–11]

[1]Eye Clinic Zurich West, Zurich, Switzerland

[2]Department of Ophthalmology, University of Zurich, Zurich, Switzerland

[3]Department of Ophthalmology, Inselspital, Bern University Hospital, University of Bern, Bern, Switzerland

[4]Department of Ophthalmology, University of Cologne, Faculty of Medicine and University Hospital Cologne, Cologne, Germany

[5]Department of Ophthalmology, Goethe-University Frankfurt, Germany

[6]Department of Dermatology, Venerology, and Allergology, University Medical Center, Ruprecht-Karls-University, Heidelberg, Germany

[7]Department of Ophthalmology, Stadtspital Zurich, Zurich, Switzerland

[8]Berner Augenklinik, Zieglerstrasse 29, Bern, Switzerland

[9]Department of Ophthalmology, University of Basel, Basel, Switzerland

[10]Institute of Molecular and Clinical Ophthalmology Basel (IOB), Basel, Switzerland

[11]Department of Genetics and Genome Biology, University of Leicester, Leicester, United Kingdom

Supplementary Online Content

Supplement to: *JAW Giger et al. Measurement Reliability and Functional Validity of Bruch's Membrane Calcification in Pseudoxanthoma Elasticum: PROPXE Study Report 2*

Content	**Page**
Supplementary Figure S1. Distinguishing Peau d'Orange Boundaries from Subretinal Drusenoid Deposits	2
Supplementary Figure S2. Comparison to Previously Published Data	3
Supplementary Figure S3. Association Between the Temporal Inner Peau d'Orange Boundary and Delayed Dark Adaptation	4
Supplementary Table S1. Inter-Reader Reliability	5
Supplementary Table S2. Inter-Visit Reliability	6
Supplementary Table S3. Inter-Eye Concordance	7
Supplementary Table S4. Association Between Age and Peau d'Orange Boundary Extents	8
Supplementary Table S5. Association Between the Temporal Inner Peau d'Orange Boundary Extent and Rod-Intercept Time (RIT)	9
Supplementary Table S6. Association Between the Superior Inner Peau d'Orange Boundary Extent and Rod-Intercept Time (RIT)	10
Supplementary Table S7. Association Between the Inferior Inner Peau d'Orange Boundary Extent and Rod-Intercept Time (RIT)	11
Supplementary Table S8. Multiple Hypothesis Testing Using the Benjamini–Hochberg (BH) Procedure	12
Supplementary Table S9. Sensitivity Analyses	13
Supplementary Methods. Non-linear Mixed Model with a Step Function	14
Supplementary Table S10. Non-linear Mixed Model with a Step Function to Describe the Relationship Between the Temporal Inner Peau d'Orange Boundary Extent and the Rod-Intercept Time (RIT)	15
References	16

Supplementary Figure S1. Distinguishing Peau d'Orange Boundaries from Subretinal Drusenoid Deposits

Annotators applied multiple criteria to distinguish peau d'orange (PdO) from subretinal drusenoid deposits (SDD). First, the characteristic patterns of the two entities differ: PdO typically appears as a fine, isoreflective dotted pattern within an area of increased reflectance (i.e., dots are isoreflective relative to the unaffected retina), whereas SDD present as round-to-oval or ribbon-like hyporeflective formations (panel B).[1] Second, the extent of angioid streaks served as a landmark for identifying the PdO inner boundary, as the longest streaks usually terminate at or near this margin (panel C).[2] Third, natural history was taken into account: a large cohort study reported that SDD occur only in eyes where the temporal extent of the PdO inner boundary is ≥19° (5.6 mm) from the optic nerve head.[1]

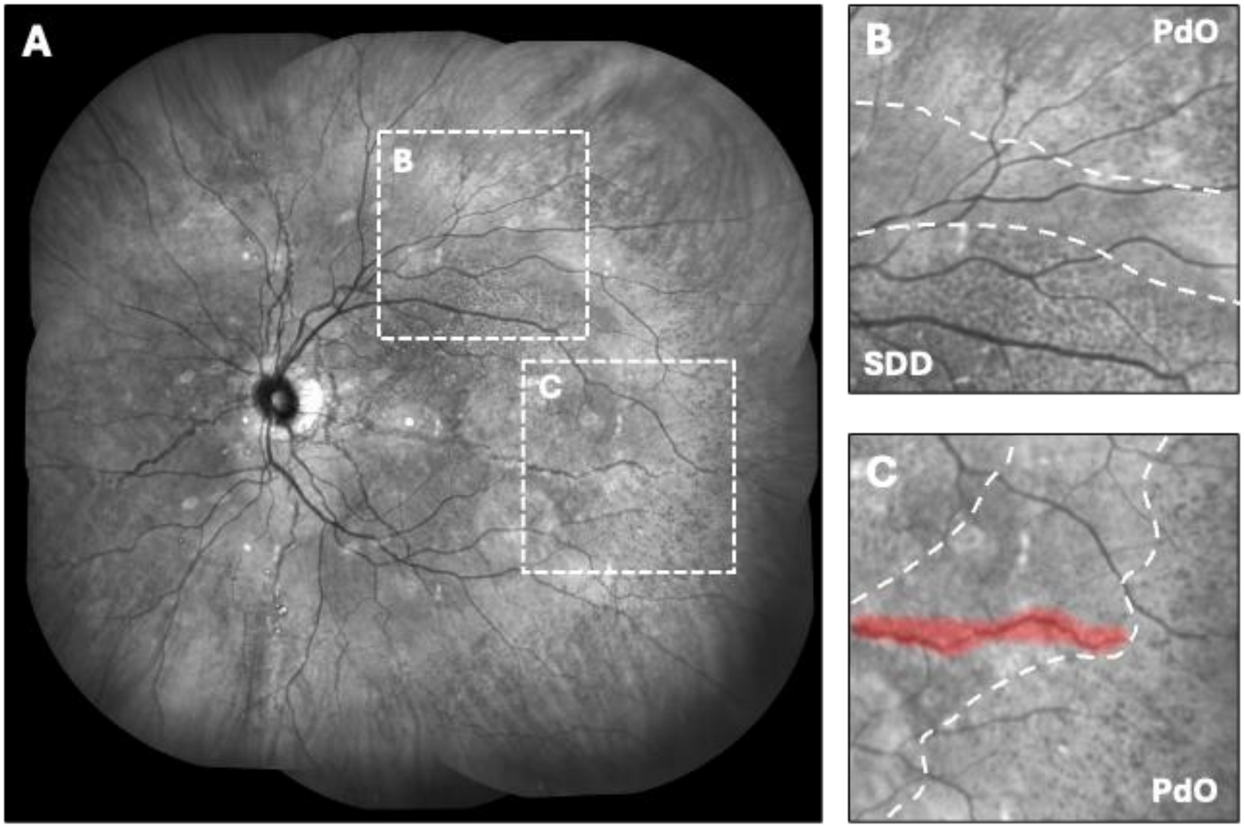

Supplementary Figure S2. Comparison to Previously Published Data

The two dot plots show the temporal inner (left plot) and temporal outer (right plot) peau d'orange boundary extents measured in our study (yellow/gold dots) and in a Dutch cohort.[3] The latter data were derived from Figure 3 in Risseeuw et al. 2021.[3]

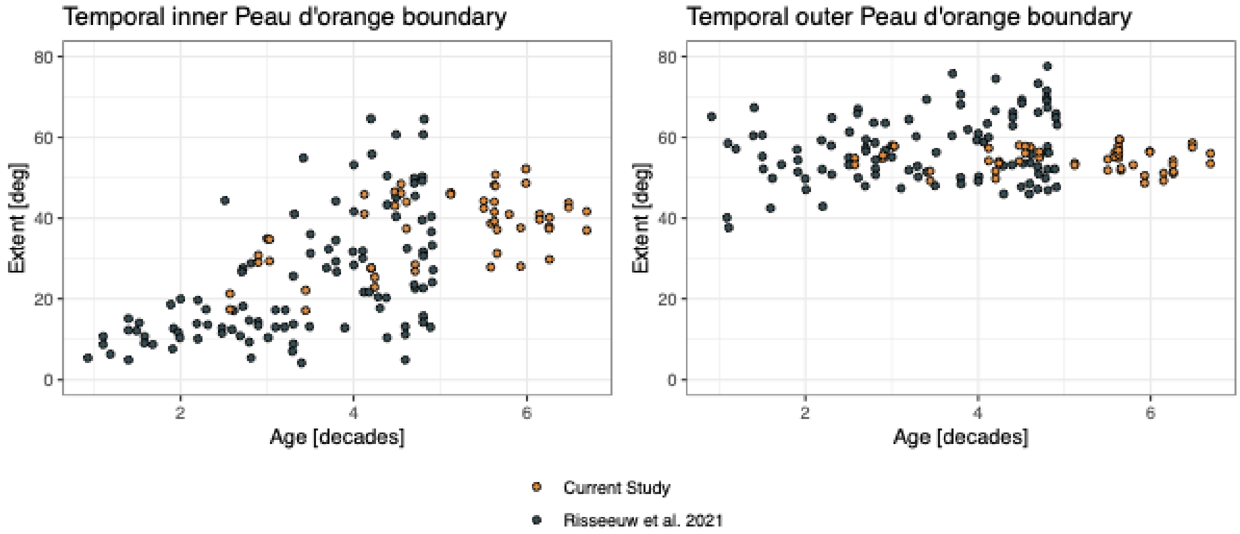

Supplementary Figure S3. Association Between the Temporal Inner Peau d’Orange Boundary and Delayed Dark Adaptation

The panels show the relationship between the temporal inner peau d’orange boundary and the rod-intercept time (RIT) as a measure of dark adaptation at 8°, 15°, and 30° eccentricity. The regression lines for the associations between the temporal inner boundary extent and RIT at 8° and 15°, respectively, were derived using a non-linear mixed model with a step function.

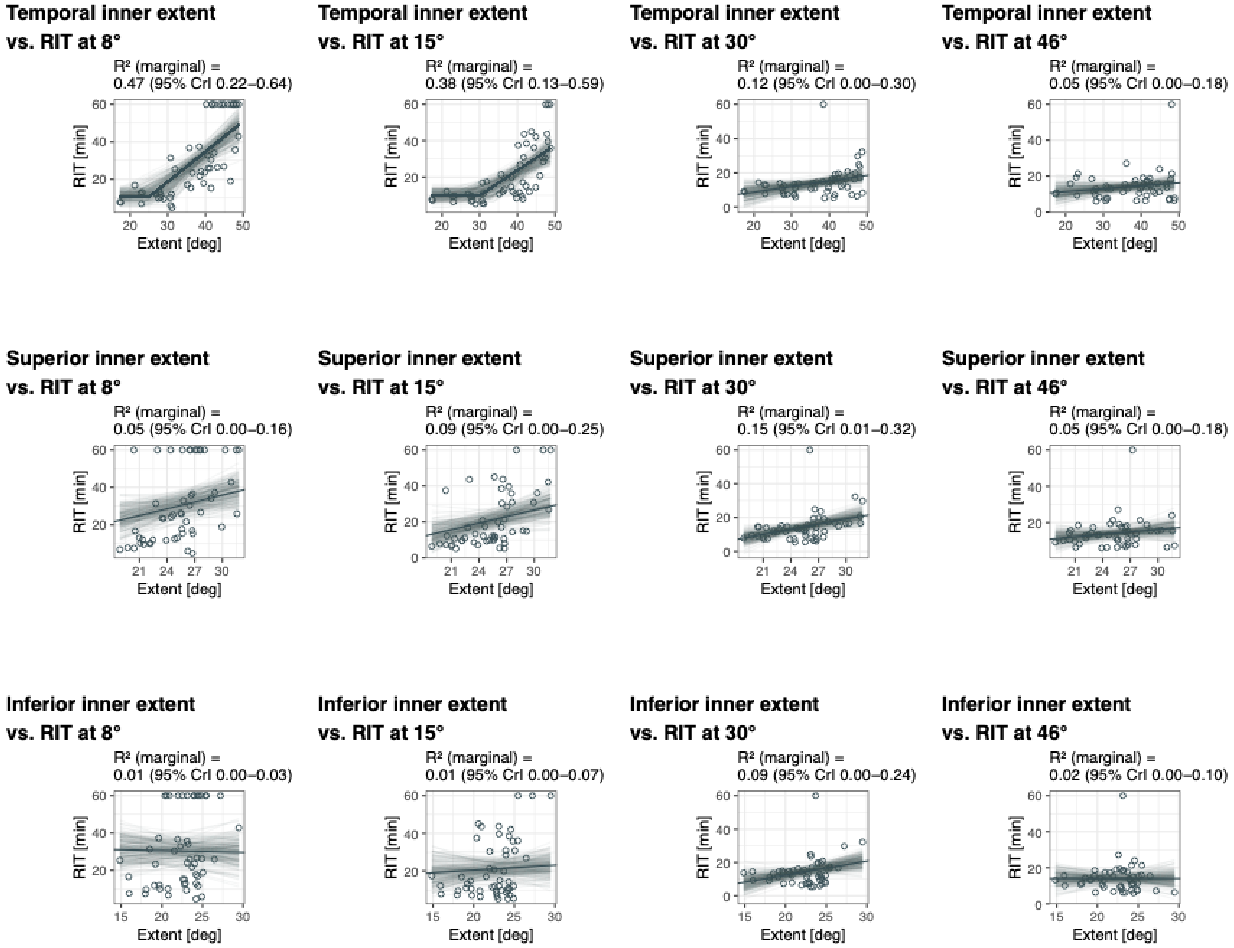

Supplementary Table S1. Inter-Reader Reliability

Visit	Meridian	Boundary	Standard Error of Measurement	Coefficient of Variation	Intraclass Correlation Coefficient (two-way random, agreement)
V1	Temporal	Inner	2.68 [2.11, 3.17]	0.07 [0.06, 0.09]	0.92 [0.89, 0.95]
		Outer	2.50 [1.36, 3.68]	0.05 [0.02, 0.07]	0.48 [0.30, 0.64]
V1	Superior	Inner	2.35 [1.86, 2.87]	0.09 [0.07, 0.11]	0.66 [0.54, 0.76]
		Outer	2.22 [1.88, 2.49]	0.06 [0.05, 0.07]	0.51 [0.32, 0.66]
V1	Inferior	Inner	2.93 [2.32, 3.47]	0.13 [0.11, 0.16]	0.39 [0.24, 0.54]
		Outer	3.09 [2.43, 3.67]	0.10 [0.08, 0.12]	0.32 [0.16, 0.48]
V2	Temporal	Inner	4.11 [3.29, 4.79]	0.11 [0.09, 0.14]	0.82 [0.74, 0.88]
		Outer	1.34 [1.11, 1.54]	0.02 [0.02, 0.03]	0.61 [0.29, 0.78]
V2	Superior	Inner	2.08 [1.60, 2.50]	0.08 [0.06, 0.10]	0.65 [0.53, 0.76]
		Outer	2.17 [1.61, 2.66]	0.06 [0.05, 0.08]	0.44 [0.24, 0.61]
V2	Inferior	Inner	2.70 [2.07, 3.30]	0.12 [0.09, 0.15]	0.43 [0.28, 0.57]
		Outer	1.92 [1.51, 2.29]	0.06 [0.05, 0.07]	0.46 [0.21, 0.65]

Supplementary Table S2. Inter-Visit Reliability

Meridian	Boundary	Standard Error of Measurement	Coefficient of Variation	Intraclass Correlation Coefficient (two-way random, agreement)
Temporal	Inner	1.97 [1.57, 2.29]	0.05 [0.04, 0.06]	0.95 [0.93, 0.97]
	Outer	1.12 [0.85, 1.36]	0.02 [0.02, 0.02]	0.86 [0.78, 0.91]
Superior	Inner	1.28 [0.99, 1.52]	0.05 [0.04, 0.06]	0.86 [0.79, 0.91]
	Outer	1.74 [1.24, 2.23]	0.05 [0.04, 0.06]	0.63 [0.47, 0.75]
Inferior	Inner	1.46 [1.12, 1.76]	0.07 [0.05, 0.08]	0.78 [0.67, 0.86]
	Outer	1.69 [1.24, 2.09]	0.05 [0.04, 0.06]	0.68 [0.53, 0.79]

Supplementary Table S3. Inter-Eye Concordance

Meridian	Boundary	Standard Error of Measurement	Coefficient of Variation	Intraclass Correlation Coefficient (two-way random, agreement)
Temporal	Inner	3.52 [2.89, 4.06]	0.09 [0.08, 0.11]	0.85 [0.77, 0.90]
	Outer	1.54 [1.12, 1.96]	0.03 [0.02, 0.04]	0.73 [0.60, 0.82]
Superior	Inner	1.56 [1.20, 1.86]	0.06 [0.05, 0.07]	0.81 [0.70, 0.88]
	Outer	1.96 [1.52, 2.34]	0.06 [0.04, 0.07]	0.50 [0.31, 0.66]
Inferior	Inner	2.36 [1.86, 2.79]	0.11 [0.08, 0.13]	0.46 [0.25, 0.62]
	Outer	2.47 [1.98, 2.88]	0.08 [0.06, 0.09]	0.32 [0.10, 0.51]

Supplementary Table S4. Association Between Age and Peau d'Orange Boundary Extents

Peau d'Orange Boundary	**Predictors**	**Estimates**	**95% CI**	**p**
Temporal inner	(Intercept)	15.17	2.01 – 28.32	**0.024**
	Age [deg/decade]	4.35	1.81 – 6.89	**0.001**
Temporal outer	(Intercept)	56.16	51.10 – 61.22	**<0.001**
	Age [deg/decade]	-0.28	-1.19 – 0.64	0.556
Superior inner	(Intercept)	20.34	14.94 – 25.74	**<0.001**
	Age [deg/decade]	1	-0.04 – 2.05	0.06
Superior outer	(Intercept)	36.05	31.48 – 40.62	**<0.001**
	Age [deg/decade]	-0.11	-0.94 – 0.72	0.788
Inferior inner	(Intercept)	18.26	13.67 – 22.84	**<0.001**
	Age [deg/decade]	0.79	-0.07 – 1.65	0.071
Inferior outer	(Intercept)	34.43	30.09 – 38.77	**<0.001**
	Age [deg/decade]	-0.43	-1.17 – 0.32	0.259

Supplementary Table S5. Association Between the Temporal Inner Peau d’Orange Boundary Extent and Rod-Intercept Time (RIT)

Temporal Inner Boundary		RIT at 8°			RIT at 15°			RIT at 30°			RIT at 46°	
Predictors	**Estimates**	**95% CI**	**p**	**Estimates**	**95% CI**	**p**	**Estimates**	**95% CI**	**p**	**Estimates**	**95% CI**	**p**
(Intercept)	-24.49	-50.98 – 2.00	0.069	-16.84	-38.75 – 5.07	0.129	-3.93	-16.87 – 9.00	0.544	6.31	-6.57 – 19.19	0.329
Extent [min/degree]	1.05	0.41 – 1.70	**0.002**	0.91	0.37 – 1.44	**0.001**	0.14	-0.22 – 0.50	0.435	0.10	-0.26 – 0.46	0.591
Age [min/decade]	3.18	-2.37 – 8.73	0.254	0.83	-3.76 – 5.41	0.719	2.60	-0.17 – 5.36	0.065	0.84	-1.92 – 3.60	0.545
Random Effects												
σ^2		33.66			23.14			43.17			50.97	
τ_{00}		172.31 PID			117.74 PID			21.53 PID			17.03 PID	
ICC		0.84			0.84			0.33			0.25	
N		26 PID			26 PID			26 PID			26 PID	
Observations		52			52			52			51	
Marginal R^2 / Conditional R^2		0.401 / 0.902			0.341 / 0.892			0.184 / 0.455			0.037 / 0.278	

Supplementary Table S6. Association Between the Superior Inner Peau d'Orange Boundary Extent and Rod-Intercept Time (RIT)

Superior Inner Boundary		**RIT at 8°**			**RIT at 15°**			**RIT at 30°**			**RIT at 46°**	
Predictors	**Estimates**	**95% CI**	**p**	**Estimates**	**95% CI**	**p**	**Estimates**	**95% CI**	**p**	**Estimates**	**95% CI**	**p**
(Intercept)	-31.99	-71.07 – 7.10	0.106	-26.91	-58.58 – 4.77	0.094	-17.61	-37.34 – 2.13	0.079	0.32	-20.28 – 20.92	0.975
Extent [min/degree]	1.16	-0.05 – 2.38	0.059	1.18	0.13 – 2.23	**0.028**	0.79	-0.02 – 1.60	0.055	0.37	-0.47 – 1.22	0.381
Age [min/decade]	6.56	0.47 – 12.64	**0.035**	3.53	-1.20 – 8.26	0.140	2.36	-0.02 – 4.74	0.052	0.86	-1.60 – 3.32	0.486
Random Effects												
σ^2		23.97			19.76			40.38			49.27	
τ_{00}		280.27 $_{\mathrm{PID}}$			164.82 $_{\mathrm{PID}}$			20.39 $_{\mathrm{PID}}$			18.57 $_{\mathrm{PID}}$	
ICC		0.92			0.89			0.34			0.27	
N		26 $_{\mathrm{PID}}$			26 $_{\mathrm{PID}}$			26 $_{\mathrm{PID}}$			26 $_{\mathrm{PID}}$	
Observations		52			52			52			51	
Marginal R^2 / Conditional R^2		0.233 / 0.940			0.188 / 0.913			0.239 / 0.494			0.048 / 0.308	

Supplementary Table S7. Association Between the Inferior Inner Peau d’Orange Boundary Extent and Rod-Intercept Time (RIT)

Inferior Inner Boundary		**RIT at 8°**			**RIT at 15°**			**RIT at 30°**			**RIT at 46°**	
Predictors	**Estimates**	**95% CI**	**p**	**Estimates**	**95% CI**	**p**	**Estimates**	**95% CI**	**p**	**Estimates**	**95% CI**	**p**
(Intercept)	-4.14	-43.11 – 34.83	0.832	-6.74	-38.68 – 25.21	0.673	-14.15	-34.31 – 6.01	0.164	10.11	-10.35 – 30.56	0.325
Extent [min/degree]	-0.25	-1.35 – 0.86	0.657	0.18	-0.80 – 1.16	0.714	0.65	-0.21 – 1.51	0.135	-0.13	-1.01 – 0.76	0.777
Age [min/decade]	7.98	1.57 – 14.40	**0.016**	4.68	-0.40 – 9.76	0.070	2.75	0.38 – 5.13	**0.024**	1.35	-1.01 – 3.71	0.256
Random Effects												
σ^2	24.03			19.84			40.07			51.10		
τ_{00}	323.46 $_{PID}$			199.69 $_{PID}$			23.70 $_{PID}$			17.23 $_{PID}$		
ICC	0.93			0.91			0.37			0.25		
N	26 $_{PID}$			26 $_{PID}$			26 $_{PID}$			26 $_{PID}$		
Observations	52			52			52			51		
Marginal R^2 / Conditional R^2	0.188 / 0.944			0.122 / 0.921			0.209 / 0.503			0.032 / 0.276		

Supplementary Table S8. Multiple Hypothesis Testing Using the Benjamini–Hochberg (BH) Procedure

Multiple hypothesis testing was addressed using the Benjamini–Hochberg (BH) procedure to control the false discovery rate (FDR). Specifically, we extracted the raw p-values for the fixed effects of interest (effect of extent) from the mixed-effects models and applied BH correction. We report both the raw p-values and the corresponding FDR-adjusted q-values in Supplementary Tables S5–S7. Covariate effects (e.g., AgeDecades) were included for confounding adjustment but were not considered part of the tested hypothesis family and therefore not subjected to FDR correction. Conclusions were based on q < 0.05 as the threshold for statistical significance.

RIT Eccentricity (Outcome)	**Meridian**	**Boundary**	**Est [95% CI]**	**p raw**	**q BH**	**Significance Bonferroni**	**Significance Benjamini–Hochberg**
8	Temporal	Inner	**1.05 [0.41, 1.70]**	**0.002**	**0.004**		*
15	Temporal	Inner	**0.91 [0.37, 1.44]**	**0.001**	**0.004**	†	*
30	Temporal	Inner	0.14 [-0.22, 0.50]	0.438	0.584		
46	Temporal	Inner	0.10 [-0.27, 0.46]	0.593	0.593		
8	Superior	Inner	1.16 [-0.05, 2.38]	0.06	0.081		
15	Superior	Inner	1.18 [0.13, 2.24]	0.029	0.081		
30	Superior	Inner	0.79 [-0.02, 1.60]	0.057	0.081		
46	Superior	Inner	0.37 [-0.48, 1.23]	0.383	0.383		
8	Inferior	Inner	-0.25 [-1.36, 0.87]	0.658	0.778		
15	Inferior	Inner	0.18 [-0.81, 1.17]	0.714	0.778		
30	Inferior	Inner	0.65 [-0.21, 1.52]	0.136	0.545		
46	Inferior	Inner	-0.13 [-1.02, 0.77]	0.778	0.778		

Supplementary Table S9. Sensitivity Analyses

To assess whether the association between peau d'orange extent and rod-intercept time (RIT) varied with age, we performed a stratified analysis, splitting participants at the median age of 55.4 years (Younger vs. Older). Only for the younger stratum, peau d'orange extent remained significantly associated with delayed RIT. The effect size was greater in younger patients than in older patients. This difference is most plausibly explained by a methodological limitation of the study: dark adaptation testing was capped at 60 minutes. This ceiling effect likely truncated the measurable range of delay in older patients, thereby attenuating the observed strength of association.

RIT Eccentricity (Outcome)	Boundary	Meridian	Age Stratum	Estimate [min/deg]	p raw
8	Inner	Temporal	Younger	**1.43 [0.75, 2.11]**	**<0.001**
8	Inner	Temporal	Older	0.73 [-0.40, 1.87]	0.194
8	Inner	Superior	Younger	0.45 [-0.41, 1.31]	0.274
8	Inner	Superior	Older	1.20 [-1.11, 3.51]	0.293
8	Inner	Inferior	Younger	-0.74 [-1.50, 0.02]	0.055
8	Inner	Inferior	Older	-0.07 [-1.98, 1.85]	0.944
15	Inner	Temporal	Younger	**1.02 [0.42, 1.62]**	**0.003**
15	Inner	Temporal	Older	0.21 [-0.37, 0.79]	0.442
15	Inner	Superior	Younger	**1.95 [0.35, 3.55]**	**0.019**
15	Inner	Superior	Older	1.00 [-0.12, 2.11]	0.077
15	Inner	Inferior	Younger	-0.01 [-1.88, 1.87]	0.994
15	Inner	Inferior	Older	0.43 [-0.42, 1.28]	0.292
30	Inner	Temporal	Younger	0.06 [-0.18, 0.29]	0.622
30	Inner	Temporal	Older	0.75 [-0.04, 1.54]	0.062
30	Inner	Superior	Younger	0.50 [-0.04, 1.04]	0.07
30	Inner	Superior	Older	1.37 [-0.28, 3.02]	0.097
30	Inner	Inferior	Younger	0.02 [-0.63, 0.66]	0.961
30	Inner	Inferior	Older	1.46 [-0.09, 3.02]	0.064
46	Inner	Temporal	Younger	-0.02 [-0.30, 0.25]	0.845
46	Inner	Temporal	Older	0.52 [-0.25, 1.29]	0.172
46	Inner	Superior	Younger	0.59 [-0.14, 1.33]	0.106
46	Inner	Superior	Older	0.23 [-1.40, 1.86]	0.765
46	Inner	Inferior	Younger	0.14 [-0.70, 0.98]	0.73
46	Inner	Inferior	Older	-0.23 [-1.78, 1.32]	0.761

Supplementary Methods. Non-linear Mixed Model with a Step Function

To describe the non-linear relationship between the temporal inner peau d'orange boundary extent and the rod-intercept time at 8° and 15° eccentricity, we fitted a Bayesian non-linear mixed-model (estimated using MCMC sampling with four chains of 2000 iterations and a warmup of 1000).

Formula: RIT ~ b0 + b1 × Age + b2 × (Extent - Omega) × step(Extent - Omega)

The following priors were used:

Parameter	Description	Prior	95% HDI of the Prior	Reasoning
b0	Intercept	normal(10, 2.5)	[5, 15]	Weakly informative prior based on RIT normal data
b1	Effect of Age	lognormal(-0.3, 0.4)	[0.27, 1.47]	Weakly informative prior based on ageing effect on RIT (per decade)[4,5]
b2	Effect of Peau d'Orange Extent	normal(0, 1.5)	[-3, 3]	Uninformative prior
Omega	Critical Extent/Step Function	normal(35, 10)	[15, 55]	Weakly informative prior based on the age range of patients in the study

Supplementary Table S10. Non-linear Mixed Model with a Step Function to Describe the Relationship Between the Temporal Inner Peau d'Orange Boundary Extent and the Rod-Intercept Time (RIT)

	RIT at 8°		**RIT at 15°**	
Predictors	**Estimates**	**Credible Interval (95%)**	**Estimates**	**Credible Interval (95%)**
Intercept [min]	10.14	5.53 – 14.78	9.32	5.02 – 13.66
Age [min/decade]	0.79	0.36 – 1.72	0.73	0.34 – 1.49
Effect of extent [min/mm]	1.48	0.76 – 2.34	1.27	0.50 – 2.75
Critical extent [mm]	27.15	17.06 – 33.09	32.56	22.64 – 40.56
Observations	52		52	
Marginal R2 / Conditional R2	0.440 / 0.902		0.328 / 0.891	

References

1. Gliem M, Hendig D, Finger RP, Holz FG, Charbel Issa P. Reticular pseudodrusen associated with a diseased Bruch membranein pseudoxanthoma elasticum. *JAMA Ophthalmol*. 2015;133(5):581-588. doi:10.1001/jamaophthalmol.2015.117

2. Pfau K, Lengyel I, Ossewaarde-van Norel J, et al. Pseudoxanthoma elasticum - Genetics, pathophysiology, and clinical presentation. *Prog Retin Eye Res*. 2024;102:101274. doi:10.1016/j.preteyeres.2024.101274

3. Risseeuw S, van Leeuwen R, Imhof SM, Spiering W, Norel JO van. The Natural History of Bruch's Membrane Calcification in Pseudoxanthoma Elasticum. *Ophthalmology science*. 2021;1(1):100001. doi:10.1016/j.xops.2020.100001

4. Oertli JM, Pfau K, Scholl HPN, Jeffrey BG, Pfau M. Establishing Fully-Automated Fundus-Controlled Dark Adaptometry: A Validation and Retest-Reliability Study. *Transl Vis Sci Technol*. 2023;12(12):18. doi:10.1167/tvst.12.12.18

5. Hess K, de Silva T, Grisso P, et al. Evaluation of Cone- and Rod-Mediated Parameters in Dark Adaptation Testing as Outcome Measures in Age-Related Macular Degeneration. *Ophthalmol Retina*. 2022;6(12):1173-1184. doi:https://doi.org/10.1016/j.oret.2022.05.018